Secondary Coordination Sphere Influences the Formation of Fe(III)-O or Fe(III)-OH in Nitrite Reduction: A Synthetic and Computational Study

Yun Ji Park,[a] Marconi N. Peñas-DeFrutos,[b] Michael J. Drummond,[a] Zachary Gordon,[a] Oscar R. Kelly,[b] Ian J. Garvey,[a] Kelly L. Gullett,[a] Max García-Melchor,[b*] and Alison R. Fout[a*]

[a]School of Chemical Sciences, University of Illinois at Urbana-Champaign, 600 S. Mathews Avenue, Urbana, IL 61801, United States.
[b]School of Chemistry, CRANN and AMBER Research Centres, Trinity College Dublin, College Green, Dublin 2, Ireland.

Supporting Information Placeholder,

ABSTRACT: The reduction of nitrite (NO_2^-) to generate nitric oxide (NO) is a significant area of research due to their roles in the global nitrogen cycle. Here we describe various modifications of the tris(5-cyclohexyliminopyrrol-2-ylmethyl)amine $H_3[N(pi^R)_3]$ ligand where the steric bulk and acidity of the secondary coordination sphere were explored in the non-heme iron system for nitrite reduction. The cyclohexyl and 2,4,6-trimethylphenyl variants of the ligand were used to probe the mechanism of nitrite reduction. While previously stoichiometric addition of nitrite to the iron(II)-species generated an iron(III)-oxo complex, changing the secondary coordination sphere to mesityl resulted in an iron(III)-hydroxo complex. Subsequent addition of an electron and two protons led to the release of water and regeneration of the starting iron(II) catalyst. This sequence mirrored the proposed mechanism of nitrite reduction in biological systems, where the distal histidine residue shuttles protons to the active site. Computational studies aimed at interrogating the dissimilar behavior of the cyclohexyl and mesityl ligand systems resulting in Fe(III)-oxo and Fe(III)-hydroxo complexes, respectively, shed light on the key role of H-bonds involving the secondary coordination sphere on the relative stability of these species.

INTRODUCTION

Nitrite (NO_2^-) and its biochemical properties are an area of significant research interest, stemming from the role of nitrite in the global nitrogen cycle, its potential to be a therapeutic for diseases affecting blood flow, and its recent classification as a ground water contaminant.[1–8] The biological reduction of nitrite to nitric oxide (NO) requires two protons and one electron and is achieved by a wide range of metalloenzymes, including heme-associated globins, molybdoflavoproteins, mitochondrial proteins, and cytochrome p450 enzymes.[1,3,5] To gain a better understanding of enzymatic nitrite reduction, structural and computational studies were performed and revealed the importance of the hydrogen bonding networks of the protein superstructure in the reaction sequence.[9–14] In cytochrome *cd1* nitrite re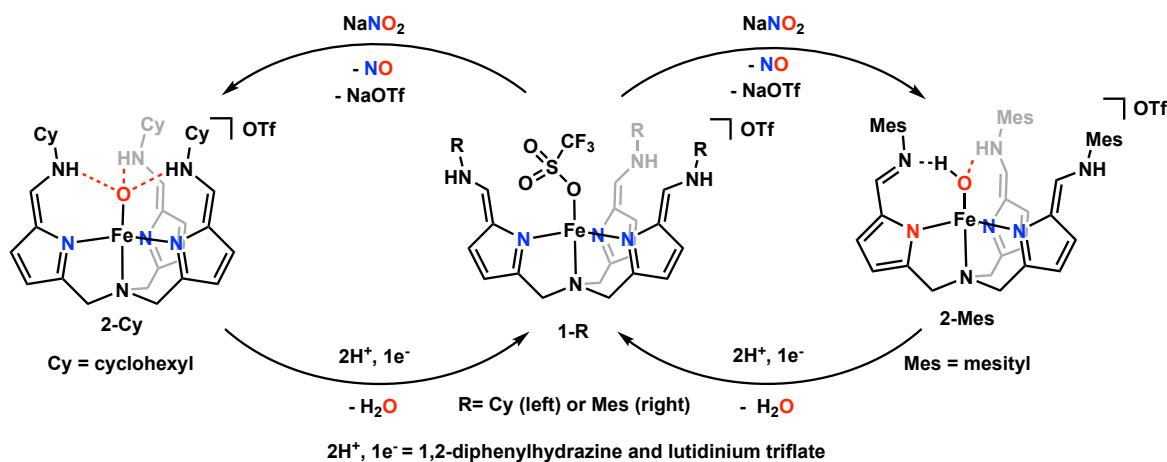ductase, for example, the distal histidine residue facilitates nitrite bonding to the metal center via a hydrogen bonding interaction and is also intimately involved in the proton-assisted reduction of nitrite.[9–12]

Several groups have described the transition metal-mediated reduction of nitrite, some of which require the addition of proton and/or electron sources, such as thiols or acids, to facilitate the reaction.[11,12,15–24] We previously reported the influence of hydrogen bonding on the reduction of nitrite, nitrate, and chlorine oxyanions.[15,23,25,26] Our work corroborated published density functional theory (DFT) studies on nitrite reduction[27,28] by demonstrating that a single hydrogen bonding interaction from the secondary coordination sphere of our tautomerizable ligand platform tris(5-cyclohexyliminopyrrol-2-ylmethyl)amine $(H_3[N(pi^{Cy})_3]$, Scheme 1) stabilizes the nitrito binding mode of nitrite. In our non-heme iron system, nitrite is readily reduced, generating a terminal iron(III)-oxo complex and $NO(g)$. Unlike other reported examples of nitrite reduction, no additional proton and/or electron source is required. These results align with those reported by Gilbertson, in which an iron pyridinediimine complex, featuring a proton-responsive secondary coordination sphere, converts nitrite to $NO(g)$.[19,20] However, in contrast to the several reports,[16,17,19–21] our system does not form an Fe-NO species unless a substoichiometric amount of nitrite is added.[23]

Given the biological significance of nitrite reduction, we sought to catalytically reduce nitrite and gain a better mechanistic understanding of its reduction in our system. Examples of heterogeneous,
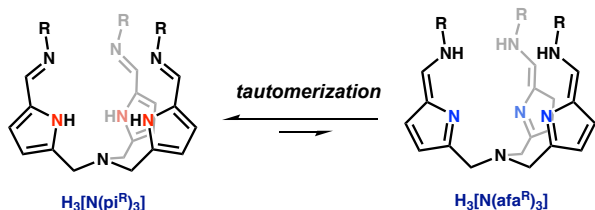
R = Cyclohexyl (Cy), Adamantyl (Ad), Phenyl (Ph), Mesityl (Mes)

Scheme 1. Ligand tautomerization.

Scheme 2. Comparison of the reduction of nitrite to **2-Cy** (left) and **2-Mes** (right) with an iron-triflate catalyst.

NaNO₂ - NO - NaOTf

Cy = cyclohexyl **2-Cy**

1-R R = Cy (left) or Mes (right)

2H⁺, 1e⁻ - H₂O

Mes = mesityl **2-Mes**

NaNO₂ - NO - NaOTf

2H⁺, 1e⁻ = 1,2-diphenylhydrazine and lutidinium triflate

homogenous, and electrocatalytic iron-based systems have been reported for the reduction of nitrite.[16,29–36] Herein, we expand our previous report of stoichiometric nitrite reduction to catalytic nitrite reduction using several variants of our ligand platform. The transfer of protons from the secondary coordination sphere to the axially bound intermediates to generate water is demonstrated and mirrors biological systems. The involvement of the secondary coordination sphere in facilitating chemical transformations is rare in synthetic inorganic systems, and accordingly provides important insights into the mechanism of nitrite reduction promoted by metalloenzymes.

RESULTS AND DISCUSSION

Catalytic Nitrite Reduction. Our group previously demonstrated the role of hydrogen bonding interactions between the secondary coordination sphere of the tripodal ligand N(pi^{Cy})₃ and ancillary substrates in a series of iron, manganese, and cobalt complexes.[23,25,37,38,39] Moreover, we reported the ability of the biomimetic non-heme iron(II) species [N(afa^{Cy})₃FeOTf]OTf (**1-Cy**), (OTf = trifluoromethanesulfonate) to bind and reduce nitrite, producing NO(g) and a terminal iron(III)-oxo species, [N(afa^{Cy})₃FeO]OTf (**2-Cy**).[23] The current investigation seeks to catalytically reduce nitrite and explore the role of the secondary coordination sphere imparted by our ligand in the reduction.

The protocol for catalytic nitrite reduction was adopted from the report describing the catalytic reduction of nitrate (NO₃⁻) and perchlorate (ClO₄⁻) by [N(afa^{Cy})₃FeOTf]OTf (**1-Cy**) in which 1,2-diphenylhydrazine (DPH) served as a 2H⁺/2e⁻ source.[25,26] Because the reduction of nitrite to nitric oxide and water requires one electron and two protons, 0.5 equiv DPH (1H⁺/1e⁻) and 1 equiv of the mild acid 2,6-lutidinium triflate (LuHOTf; 1H⁺) were needed as the source of the requisite protons and electron, shown in Scheme 2. The turnover number (TON) of the reaction was determined by flowing N₂ through the reaction vessel into a separate flask containing cobalt-tetraphenylporphyrin ((TPP)Co), a known NO(g) scavenger (see SI for full experimental details),[40] as previously utilized to confirm the formation of NO (g).[24,41,42] When 0.25 equiv of **1-Cy** was added, 0.47 equiv of the (TPP)Co was converted to (TPP)Co(NO) corresponding to a TON of 1.9 (see Table 1 and Figure S1). Control experiments under the same conditions using FeOTf₂(MeCN)₂ or

without iron present converted 0.22 equiv and 0.13 equiv of the (TPP)Co to (TPP)Co(NO), respectively (Figures S2 and S3). The poor catalytic performance of **1-Cy** was further investigated. Upon analysis by ¹H NMR spectroscopy of the crude catalytic reaction, the primary species in solution was identified as the protodemetallated ligand salt N(pi^{Cy})₃ • 3HOTf (Figure S4).[25] Protodemetallation of the catalyst was alleviated by slowly adding a solution of LuHOTf to the reaction mixture with a syringe pump, which improved the TON to 6.7 (Figure S5).

To disfavor the protodemetallation of the ligand in acidic media and use of a syringe pump, the cyclohexylamine ligand was replaced by aniline to include a more acidic secondary coordination sphere (pKa = 10.64 vs 4.6, respectively).[43] Because of the modular synthesis of our ligand, we targeted the previously synthesized N(pi^{Ph})₃ ligand.[38] The analogous iron(II)-triflate species [N(afa^{Ph})₃FeOTf]OTf (**1-Ph**) was generated from the metalation of the ligand with Fe(OTf)₂(MeCN)₂. Under the previously described catalytic conditions, **1-Ph** performed marginally better, with 0.55 equiv of the (TPP)Co converted to (TPP)Co(NO) and a TON of 2.2 (Figure S8).

In order to further improve the catalytic reduction of nitrite and explore the role of the secondary coordination sphere in catalysis, the secondary coordination sphere was modified to increase its steric bulk. The adamantylamine (Ad) and 2,4,6-trimethylaniline (Mes) ligand variants and their corresponding iron(II)-triflate complexes ([N(afa^{Ad})₃FeOTf]OTf, **1-Ad**; and [N(afa^{Mes})₃FeOTf]OTf, **1-Mes**) were synthesized following the previously described protocol.[23,37,39] Yellow crystals of **1-Mes** suitable for X-ray diffraction were grown from a concentrated tetrahydrofuran solution layered with diethyl ether. Refinement of the data revealed a five-coordinate iron(II) center in pseudo-trigonal bipyramidal geometry, with a triflate anion bound *trans* to the apical nitrogen of the tripodal ligand (Figure 2). The Fe–N$_{apical}$ (2.247 Å) and Fe–N$_{pyrrole}$ distances (2.074 – 2.110 Å) composing the equatorial plane were similar to those of the previously reported iron(II)-triflate species, **1-Cy**.[39] Further analysis of intraligand bond distances revealed that all three arms of the ligand had tautomerized to the azafulvene-amine binding mode, with the two C=N stretches observed in the solid-state IR spectrum assigned to asymmetric binding of the arms of the ligand to the iron center (Figure 1). For these nitrite reduction studies, the adamantyl

Figure 1. Crystal structures with ellipsoids at the 50 % probability level. Selected hydrogen atoms, solvent molecules, and counteranions have been omitted for clarity.
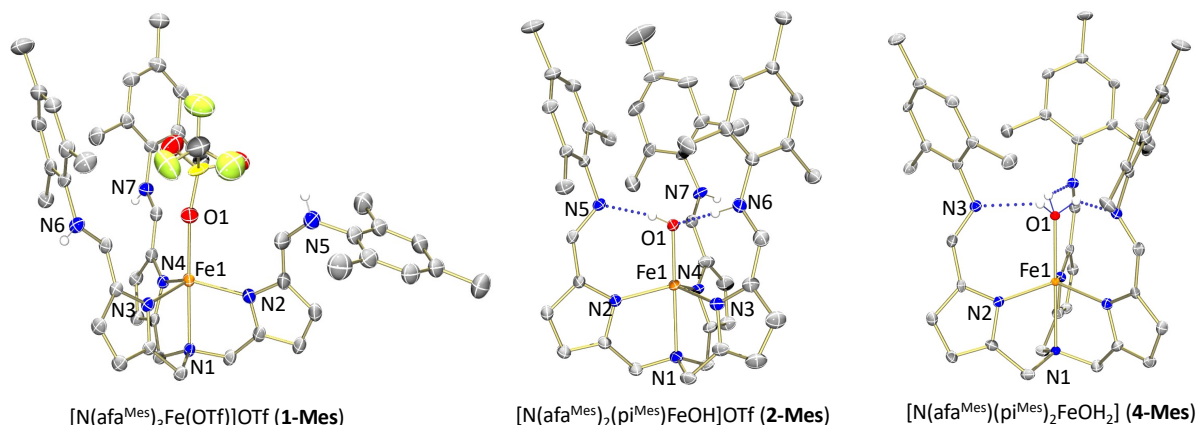

[N(afa^Mes)₃Fe(OTf)]OTf (**1-Mes**)   [N(afa^Mes)₂(pi^Mes)FeOH]OTf (**2-Mes**)   [N(afa^Mes)(pi^Mes)₂FeOH₂] (**4-Mes**)

Table 2. Selected structural parameters of the crystal structures of complexes **1-Mes**, **2-Mes**, and **4-Mes**.

Bond	1-Mes (Å)	2-Mes (Å)	4-Mes (Å)
Fe1–N1	2.247(3)	2.2492(12)	2.253(8)
Fe1–N(pyr)	2.072(3) – 2.111(3)	2.0079(13) – 2.0398(14)	2.294(5)
Fe1–O1	2.138(6)	1.8538(11)	2.112(7)
$\nu_{C=N}$	1621 ; 1636 cm⁻¹	1634 ; 1651 cm⁻¹	1616 ; 1643 cm⁻¹
Magnetic moment (μ_B)	5.52(6)	5.94(9)	—ª
τ_5-parameter	0.80(5)	0.99(80)	—ᵇ

ª A reliable magnetic moment could not be obtained for complex **4-Mes** due to its insolubility. Due to the C₃-symmetric nature of this complex and accurate τ_5 could not be calculated.

variant served as a bulkier cyclohexyl analogue, while the mesityl variant served as a bulkier phenyl analogue. **1-Ad** and **1-Mes** were tested for their catalytic competence, and both species reached the maximum TON of 4 (Figures S13 and S17). While catalysis could be improved through optimization, we merely wanted to understand the influence of the secondary sphere on the reaction and not the overall catalyst performance. Thus, we concluded that increasing the steric bulk of the secondary coordination sphere was more important for improving catalysis than increasing the ligand pKa (pKa= 10.6 and 4.4 for 1-adamantylamine and 2,4,6-trimethylaniline, respectively).

Table 1. Catalytic nitrite reduction. Catalyst loadings were 25 mol % and were run for 8 h.

Catalyst	(TPP)CoNO (equiv)	TON
1-Cy	0.47	1.9
1-Ph	0.55	2.2
1-Ad	1	4.0
1-Mes	1	4.0
None	0.13	-
FeOTf₂(MeCN)₂	0.22	-

Role of the Secondary Coordination Sphere in Catalysis. To investigate the mechanism of catalytic nitrite reduction, **1-Mes** was employed as a model catalyst because of its crystallinity and isolability compared to **1-Ad**.

The stoichiometric reduction of nitrite was performed using **1-Mes**. Upon the addition of [NⁿBu₄][NO₂] to a solution of **1-Mes**, an instantaneous color change from yellow to brown was observed, consistent with the oxidation of the iron(II) starting material. Following workup, the product (**2-Mes**) was isolated as a brown crystalline solid. Analysis of **2-Mes** by ¹H NMR spectroscopy revealed

two broad resonances at 77.16 and 60.64 ppm (Figure S18), similar to the resonances observed in the ^{1}H NMR spectrum of the previously reported iron(III)-oxo complex, 2-Cy.[23] The solution magnetic moment of 2-Mes, determined by the Evan's method (μ_{eff} = 5.94(9) μ_B), was consistent with a high-spin, S = 5/2, iron(III) center. Although the ^{1}H NMR spectrum of 2-Mes suggested a C$_3$-symmetric species, the solid-state IR spectrum contained two C=N stretches at 1634 and 1651 cm^{-1} (Table 2).

To provide a more definitive understanding of the bonding in 2-Mes, this complex was characterized by solid-state structural analysis. Refinement of the data revealed that 2-Mes is best described as a terminal iron(III)-hydroxo ([N(afa^{Mes})$_2$(pi^{Mes})FeOH]OTf, 2-Mes) in a pseudo-trigonal bipyramidal geometry with a hydroxide bound *trans* to the apical nitrogen of the tripodal ligand (Figure 1) which is consistent with the τ_5-parameter (see Table 2).[44] Hydrogen bonding between one amine moiety of the secondary coordination sphere and the oxygen of the hydroxo ligand was observed. Another arm exhibited positional disorder, where the amine was either pointing inward toward the iron-hydroxo moiety (not shown in Figure 1) or oriented to point away from the iron-hydroxo moiety. The crystal structure of 2-Mes demonstrates that both tautomeric forms of the arms of the ligand are present based on the intraligand bond distances and the two C=N stretches in the solid-state IR spectrum (Figure S23).

The Fe1–O1 distance of 1.8539(13) Å in 2-Mes was longer than the Fe–O distance of 2-Cy (1.8079(9) Å),[23] consistent with its formulation as a hydroxo rather than an oxo species, but was shorter than that of Borovik's iron(III)-hydroxo (1.9315(17) Å),[45] presumably due to hydrogen bonding between the hydroxo and the pendant imine in the secondary coordination sphere. The other two arms of the ligand were in the azafulvene-amine tautomeric form and were also engaged in hydrogen bonding interactions. These results suggest that the more acidic and sterically encumbered secondary coordination sphere in 2-Mes does, in fact, influence the reactivity at the iron center, as evidenced by the generation of an iron(III)-hydroxo rather than an iron(III)-oxo, as in the case with the cyclohexyl ligand variant. The formation of an iron(III)-hydroxo is also consistent

with one proposed pathway of biological nitrite reduction whereby an iron(III)-hydroxo and nitric oxide are generated.[10,27,28]

In nitrite reduction of biological systems, the iron(III)-hydroxo is subsequently protonated and reduced to form water and an iron(II) species. To further explore this reactivity in our system, two possible pathways for the reduction of 2-Mes to 1-Mes were proposed (Scheme 3). The addition of a proton (HOTf) to 2-Mes resulted in a new paramagnetic product, 3-Mes, as assayed by ^{1}H NMR spectroscopy (Figure S20). Additional characterization by mass spectrometry confirmed the formation of doubly charged protonated complex ([N(afa^{Mes})$_2$(pi^{Mes})FeOH$_2$]$^{2+}$, Figure S21), leading to the formulation of 3-Mes as the iron(III)-aquo mixed-ligand tautomer [N(afa^{Mes})$_2$(pi^{Mes})Fe(OH$_2$)]OTf$_2$. Moreover, this formulation was consistent with the C=N stretches in the solid-state IR spectrum, showing two tautomeric forms of the ligand and an O–H stretch at 3205 cm^{-1}. Subsequent addition of 0.6 equiv DPH to 3-Mes, which had been generated *in situ*, resulted in clean conversion to 1-Mes (Scheme 3, A-2) and the generation of water (0.80 equiv quantified via Karl Fisher titration, Table S1).

In the alternative pathway, KC$_8$ was added to 2-Mes resulting in the formation of a new paramagnetic iron(II) species (Scheme 3, B-1). Analysis of the species by ^{1}H NMR spectroscopy revealed paramagnetic resonances ranging from –4.04 ppm to 29.79 ppm (Figure S22). Unfortunately, the low solubility of the complex precluded the determination of its magnetic moment by the Evan's method. To unambiguously establish the identity of the iron-containing species, crystals suitable for X-ray diffraction were grown from slow diffusion of hexanes into a concentrated tetrahydrofuran solution. Refinement of the data revealed a pseudo-trigonal bipyramidal iron(II) center situated on a C$_3$-axis that included the apical nitrogen of the ligand, the iron center, and an oxygen atom. Positioning a hydrogen atom in the electron density map aided in confirming the presence of a hydrogen atom next to the axially bound oxygen (Figure 1), and displaying hydrogen bonding interactions with the pendant imine of the secondary coordination sphere. Despite the C$_3$-symmetry observed in the crystal structure, two C=N stretches at 1616 and 1643 cm^{-1} were observed in the solid-state IR spectrum, suggesting both tautomeric forms of the arms of the ligand were present, similar to

Scheme 3. Mechanistic insights into the nitrite reduction reaction.
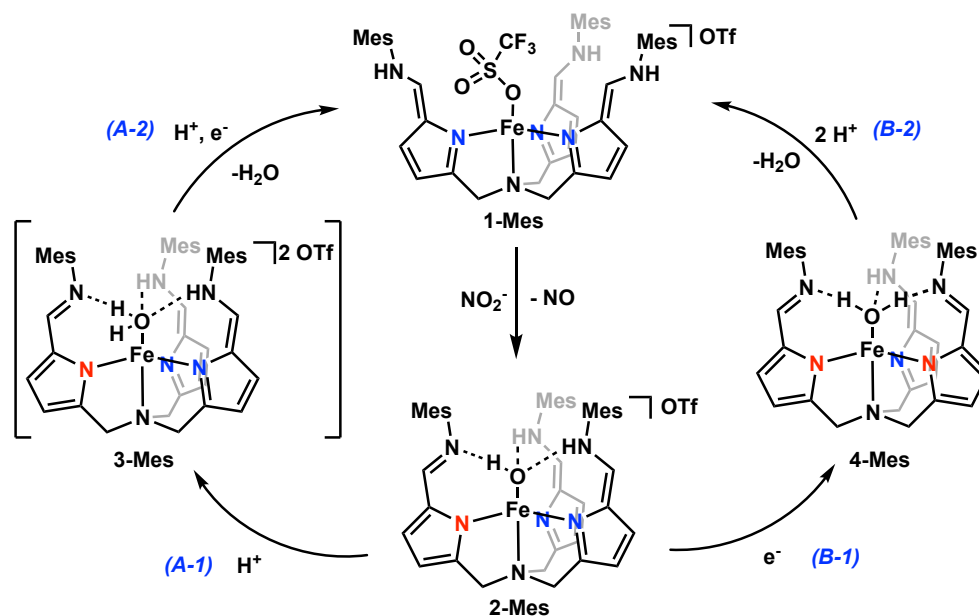
the previously reported iron(II)-hydroxo complex $N(pi^{Cy})(afa^{Cy})_2FeOH$ (C=N stretches at 1624 and 1655 cm^{-1}). Our group has also reported a similar complex featuring 2,6-diisopropylphenyl as the capping group of the secondary coordination sphere, which was assigned as an iron(II)-aquo complex based on the long Fe–O bond (2.107(2) Å). Accordingly, we proposed that **4-Mes** is best described as $N(afa^{Mes})(pi^{Mes})_2Fe(OH_2)$ because of its Fe–O bond length of 2.112(7) Å. Moreover, this result suggests that reduction from **2-Mes** to **4-Mes** not only resulted in the electron transfer to the metal center but also protonation of the bound substrate, generating an aquo ligand from the hydroxo ligand. Finally, treatment of **4-Mes** with 2.1 equiv HOTf cleanly regenerated **1-Mes** upon loss of water (1.05 equiv), as confirmed by Karl-Fisher titration (Table S1).

Computational Studies. To gain further understanding of the dissimilar behavior of the Mes and Cy ligands in this system (Scheme 2), DFT calculations at the ωb97xd level were carried out. See Materials and Methods Section for details.

According to experiments, the nature of complexes **2-Cy** and **2-Mes** is strikingly different; the former is an Fe^{III}-oxo with the three arms of the ligand H-bonded to the oxo moiety, while the latter is an Fe^{III}-hydroxo species with positional disorder in one arm. To shed light on these observations, the structures of plausible conformers in the oxo and hydroxo complexes bearing Mes and Cy ligands were optimized considering three and two ligand arms pointing inwards, all as high-spin species with S = 5/2, as confirmed experimentally (Table 2). Attending to the relative Gibbs energies calculated in acetonitrile, the structures with the three arms pointing inwards (*closed* structures) are predicted to be much more stable than the ones with one arm rotated (*open* structures). See Figure S24 for the optimized structures. Furthermore, the energy difference between the *open* and *closed* structures was found to be higher for **2-Cy** than for **2-Mes** (*i.e.* 8.5 vs 5.9 kcal mol^{-1}).

Further insight was provided by the non-covalent interaction (NCI) analysis depicted in Figure 2 (see SI for details),[46] which indicates that H-bonds are the main attractive interactions (blue and green colors) with their relative strength ranked according to the electron density, $\rho(r)$. In the case of **2-Cy**, only one type of H-bond could be identified, corresponding to the N–H⋯O–Fe interaction (Figure 2, top). Conversely, **2-Mes** displayed two types of H-bonds (Figure 2, bottom) with the most attractive one being the N⋯HO–Fe interaction, which is substantially stronger than the other two N–H⋯O(H)–Fe interactions (see Figure S25). Interestingly, the NCI plots reveal that the H-bonds in **2-Cy** have intermediate strength between the two types present in **2-Mes**. Consequently, the loss of one H-bond associated with the rotation of the ligand arms must have a different energetic cost for **2-Mes** and **2-Cy**. Specifically, upon rotation of one ligand arm, a weaker N–H⋯O(H)–Fe interaction is lost for **2-Mes** relative to the N–H⋯O–Fe interaction lost for **2-Cy**, making the rotation more favored for **2-Mes**.

Another important factor in the stability of the hydroxo and oxo complexes is the different steric requirement induced by the Mes and Cy ligands. This can be assessed by inspecting the right-hand side of the NCI plots shown in Figure 2, which clearly display more repulsive interactions for the complex with the bulkier Mes groups, as expected. Hence, we conclude that the bulkier nature of the Mes groups also contributes to reduce the energy gap between the *closed* and *open* structures.

Theoretical calculations also confirmed that there is a switch in stability between the oxo and hydroxo species depending on the ligand. More specifically, our results predict that the crystallized oxo

complex **2-Cy** is *ca.* 1 kcal mol^{-1} lower in energy than its hydroxo analogue, whereas the hydroxo complex **2-Mes** is more stable than the putative oxo complex by *ca.* 2 kcal mol^{-1} (Figure 3A). While we acknowledge that we are dealing with energy differences which are within the DFT error, we note our theoretical results are in good agreement with the different nature of complexes **2-Cy** and **2-Mes**, characterized experimentally by X-ray diffraction.

In addition, we found that the Fe–O distance in the structure with the Mes ligand is substantially shorter than in the hydroxo complex (1.756 vs 1.840 Å); this is suggestive of a stronger electron donation from the oxo group, which leads to the elongation of the Fe–N distance in its *trans* position due to the higher *trans* influence of the oxo group compared to the hydroxyl.[47] The optimized structures also reveal that the migration of the H atom induces the tautomerization of the ligand, as indicated by the selected C–C, C–N and Fe–N distances shown in Figure 3A.
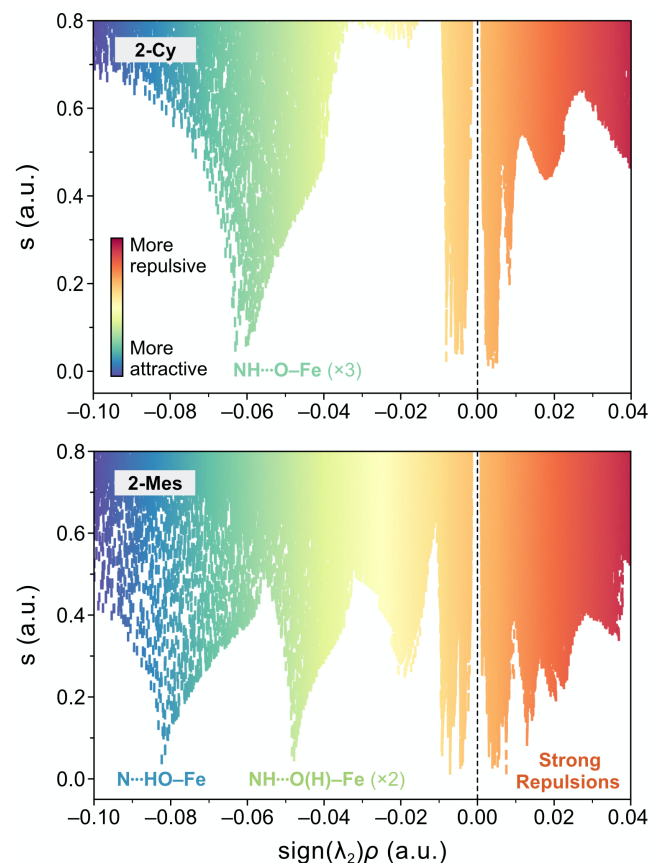

Figure 2. Analysis of the non-covalent interactions (NCIs) present in **2-Cy** (top) and **2-Mes** (bottom), highlighting the main H-bond interactions. NCI plots represent the reduced density gradient (s) as a function of the electron density ρ multiplied by the sign of the second eigenvalue of the Hessian matrix (sign(λ_2)ρ), which effectively displays the NCIs as distinct peaks. Colder/warmer colors depict attractive/repulsive interactions.

A

2-Mes-OH
$\Delta G_{(MeCN)} = 0.0$

2-Mes-oxo
$\Delta G_{(MeCN)} = 2.2$

B

LP N → BD* OH
$E_{SOPT} = -37.0$ (Mes)
-46.6 (Cy)

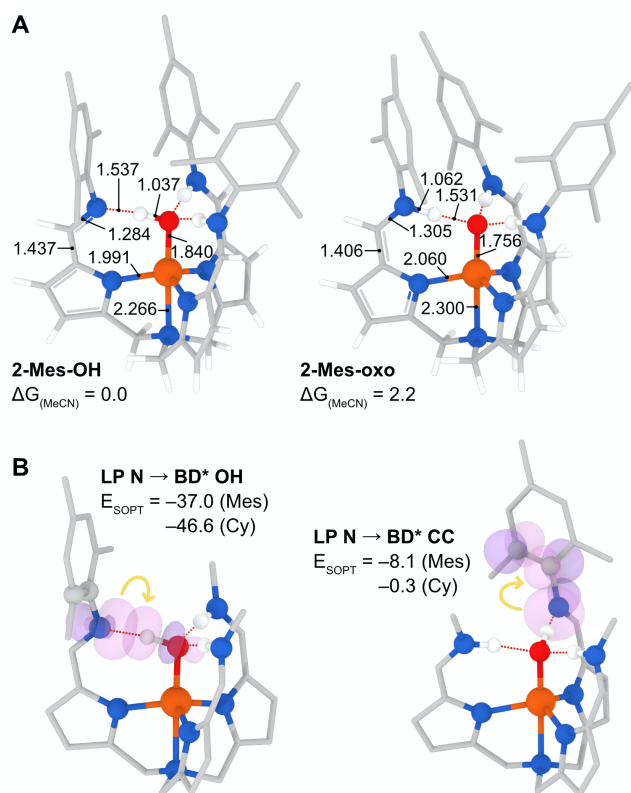LP N → BD* CC
$E_{SOPT} = -8.1$ (Mes)
-0.3 (Cy)

Figure 3. A) Optimized structures of the hydroxo (left) and oxo (right) complexes with the Mes ligand, including relevant distances in Å. Note that most of H atoms have been omitted for clarity. Relative Gibbs energies in acetonitrile, ΔG_{MeCN}, are given in kcal mol^{-1}. B) Selected donor-acceptor interactions (isovalue = 0.07 a.u) found through a natural bonding orbital (NBO) analysis. The calculated second-order perturbation theory energies, E_{SOPT}, associated to the donor-acceptor interactions in **2-Mes** are given in kcal mol^{-1}. The E_{SOPT} values for the Cy analogue are also provided for comparison. Note that the Mes ligands in the structures have been simplified with a C atom for clarity.

The higher stability of **2-Mes** compared with its oxo analogue can be explained by the higher acidity of the ligand bearing aromatic substituents, as we detail in the following: To demonstrate this, we performed a natural bonding orbital (NBO) and second order perturbation theory (SOPT) analyses on the optimized structures of the hydroxo complexes with the Mes and Cy ligands (Figure 4B and Figure S26). NBO analysis indicates that the H-bond interaction between the N-ligand and the OH group involves the electron donation from the lone pair (LP) of the N to an antibonding (BD*) orbital of the OH. Remarkably, the computed energies for this interaction, E_{SOPT}, substantially differ between the non-observed Cy-OH species and the observed Mes-OH derivative (**2-Mes**), i.e. -46.6 and -37.0 kcal mol^{-1}, respectively. Given that a strong H-bond makes the OH group more labile, the higher that interaction energy the less stable the hydroxo species will be, which is in line with experimental observations. Furthermore, in the case of the Mes ligand, the N-LP is delocalized through the Mes ring via electron donation into a C_{Mes}–C_{Mes}-BD* orbital ($E_{SOPT} = -8.1$ kcal mol^{-1}). This delocalization weakens the aforementioned H-bond interaction, stabilizing the hydroxo form over the oxo for the Mes ligand.

Finally, we modelled the interconversion between the oxo and hydroxo complexes, which consists of a simple proton transfer from

the axial oxygen to the nitrogen ligand. Importantly, the calculated energy barriers for both ligands were almost negligible (i.e. 1.0 and 1.5 kcal mol^{-1} for **2-Cys** and **2-Mes**, respectively), indicating that the formation of the different species is governed by their relative thermodynamic stability, as discussed above. However, we note that considering only the isolated cationic complexes may not provide an accurate description of the thermodynamic stability of the different species in solution. This is particularly important in reactions where anions or solvents like $^-$OTf, MeCN or THF are present in solution, as these species can act as H-bond acceptors, and therefore, provide stabilizing interactions which may be important. For example, both X-ray structures of **1-Mes** and **2-Mes** (Figure 1) were obtained from the crystallization in concentrated solutions of THF, where it is very likely that the rotated arm can establish a H-bond with the solvent or the triflate anions (see extended X-ray structure of **1-Mes** in Figure S27). To illustrate this and assess the influence of the solvent on the relative stability of the open and closed structures of **2-Mes**, we modeled these structures in the presence of an explicit THF molecule H-bonding to the outward-facing ligand arm. As expected, the addition of the THF molecule resulted in a considerable reduction in the energy difference between the two configurations, i.e. from 5.9 to only 1.1 kcal mol^{-1} in favor of the closed structure. This narrow energy difference not only explains the coexistence of both conformers in the X-ray structure obtained for **2-Mes**, but also warns on the key role that H-bond interactions in the second coordination sphere may play, as seen in enzymatic reductions in biological systems.

CONCLUSIONS

Due to the classification of nitrite as a groundwater contaminant, understanding the reduction of nitrite in biological and homogenous systems is of great importance. The nitrite reduction described herein represents a mild reaction sequence that was rendered catalytic with the appropriate proton and electron sources to produce water and NO(g). The iron catalyst features a secondary coordination sphere that is involved in the reduction of nitrite, forming an iron(III)-hydroxo species, which releases water upon the addition of an electron and two protons. Comparing the mesitwith and cyclohexyl variants has provided insight into the role of the secondary coordination sphere and allowed to improve catalytic reactivity. In addition, DFT calculations and electronic structure analyses identify H-bond interactions, and steric and electronic effects in the second coordination sphere as the main determinant factors in the stability of these species.

MATERIALS AND METHODS

All manipulations were carried out in the absence of water and dioxygen using standard Schlenk techniques or in an MBraun inert atmosphere drybox under a dinitrogen atmosphere. All glassware was oven dried for a minimum of 8 h and cooled in an evacuated antechamber prior to use in the drybox. Solvents were dried and deoxygenated on a Glass Contour System (SG Water USA, Nashua, NH) and stored over 4 Å molecular sieves purchased from Strem prior to use. Celite 545 (J. T. Baker) was heated to 100°C under dynamic vacuum for 24h prior to use in the drybox. H$_3$(tpa^{CO}),[39] Fe(OTf)$_2$(MeCN)$_2$,[39] and lutidinium triflate (LuHOTf)[48] were prepared according to literature procedures. Chloroform-d, benzene-d$_6$ and acetonitrile-d$_3$ were purchased from Cambridge Isotope Laboratories and were degassed and stored over 4 Å molecular sieves prior

1
2
3
4
5
6
7
8
9
10
11
12
13
14
15
16
17
18
19
20
21
22
23
24
25
26
27
28
29
30
31
32
33
34
35
36
37
38
39
40
41
42
43
44
45
46
47
48
49
50
51
52
53
54
55
56
57
58
59
60

to use. Potassium hydride was purchased from Sigma-Aldrich washed with hexanes to remove mineral oil, and dried under reduced vacuum prior to use. Ferrous chloride was purchased from Strem and used as received. 2,4,6,-Trimethylaniline, formic acid, lithium oxide, triflic acid, and sodium nitrite were purchased from Sigma-Aldrich and used as received. Tetrabutylammonium nitrite was purchased from Sigma-Aldrich and recrystallized from a concentrated THF solution layered with hexanes at –35°C. 1-Adamantylamine and 1,2-Diphenylhydrazine (DPH) were purchased from Oakwood Chemical with DPH being recrystallized from a concentrated diethyl ether solution layered with hexanes at –35°C. Cobalt(II) tetraphenylporphyrin was purchased from Frontier Scientific and used as received.

NMR Spectra were recorded at room temperature on a Varian spectrometer operating at 500 MHz (^{1}H NMR), 126 MHz (^{13}C NMR), and 470 MHz (^{19}F NMR) and referenced to the residual solvent resonance (δ in parts per million, and J in Hz). Solid-state infrared spectra were measured using a PerkinElmer Frontier FT-IR spectrophotometer equipped with a KRS5 thallium bromide/iodide universal attenuated total reflectance accessory. Elemental analysis was performed by the University of Illinois at Urbana-Champaign School of Chemical Sciences Microanalysis Laboratory in Urbana, IL. Analysis with mass spectrometry was performed by University of Illinois at Urbana-Champaign School of Chemical Sciences Mass Spectrometry Laboratory. Electrospray ionization mass spectrometry (ESI) was recorded on a Waters Synapt G2-Si ESI/LC-MS instrument at Data of crystal structures were collected on a Bruker D8 Venture Duo or Bruker X8ApexII diffractometer at the George L. Clark X-Ray Facility and 3M Material Laboratory at the University of Illinois at Urbana-Champaign. Crystal structures have been deposited to the Cambridge Structural database, CCDC 1842647-1842651. The quantification of water was performed by an Aquatest CMA Karl Fischer Coulometric Titrator from Photovolt Instruments with HYDRANAL from Fluka Analytical.

Catalytic Nitrite Reduction with [N(afa^{Cy})$_3$Fe(OTf)]OTf (1-Cy)

A 50 mL three-neck flask was charged with NaNO$_2$ (0.0026 g, 0.038 mmol, 1.25 equiv), 1,2-diphenylhydrazine (0.0056 g, 0.03 mmol, 1 equiv), 15 mg of MgSO$_4$, and 5 mL of acetonitrile. In another 50 mL three-neck flask, cobalt(II) tetraphenylporphyrine (CoTPP) (0.0206 g, 0.03 mmol, 1 equiv) was dissolved in approximately 25 mL of DCM. The 50mL three-neck flasks were connected with tubing and purged with nitrogen for 10 min. [N(afa^{Cy})$_3$Fe(OTf)]OTf (0.0072 g, 0.0077 mmol, 0.25 equiv) in 1 mL of acetonitrile was added via a Hamilton Sample Lock syringe to the mixture of NaNO$_2$ and 1,2-diphenylhydrazine. After stirring for 10 min, lutidinium triflate (0.0142 g, 0.055 mmol, 1.8 equiv) in 1 mL of acetonitrile was added to the reaction mixture via a Hamilton Sample Lock syringe. 1 mL of aliquot was removed from the solution of CoTPP to analyze the amount of CoTPP-NO after the reaction was stirred for 8 hours. Characterization by ^{1}H NMR spectroscopy showed that almost 0.47 equiv of Co-TPP was converted to CoTPP-NO (Figure S1).

Catalytic Nitrite Reduction with Fe(OTf)$_2$(MeCN)$_2$

A 50 mL three-neck flask was charged with NaNO$_2$ (0.0026 g, 0.038 mmol, 1.25 equiv), 1,2-diphenylhydrazine (0.0056 g, 0.03 mmol, 1 equiv), 15 mg of MgSO$_4$, and 5 mL of acetonitrile. In another 50 mL

three-neck flask, cobalt(II) tetraphenylporphyrine (CoTPP) (0.0206 g, 0.03 mmol, 1 equiv) was dissolved in approximately 25 mL of DCM. The 50mL three-neck flasks were connected with tubing and purged with nitrogen for 10 min. A clear solution of Fe(OTf)$_2$(MeCN)$_2$ (0.0034 g, 0.0077 mmol, 0.25 equiv) in 1 mL of acetonitrile was added via a Hamilton Sample Lock syringe to the mixture of NaNO$_2$ and 1,2-diphenylhydrazine. After stirring for 10 min, lutidinium triflate (0.0142 g, 0.055 mmol, 1.8 equiv) in 1 mL of acetonitrile was added to the reaction mixture via a Hamilton Sample Lock syringe. 1 mL of aliquot was removed from the solution of CoTPP to analyze the amount of CoTPP-NO after the reaction was stirred for 8 hours. Characterization by ^{1}H NMR spectroscopy showed that 0.22 equiv of Co-TPP was converted to CoTPP-NO (Figure S2).

Procedure for Control Reaction of Catalytic Nitrite Reduction (8 hours, Table 1)

A 50 mL three-neck flask was charged with NaNO$_2$ (0.0026 g, 0.038 mmol, 1.25 equiv), 1,2-diphenylhydrazine (0.0056 g, 0.03 mmol, 1 equiv, 15 mg of MgSO$_4$, and 5 mL of acetonitrile. In another 50 mL three-neck flask, cobalt(II) tetraphenylporphyrine (CoTPP) (0.0206 g, 0.03 mmol, 1 equiv) was dissolved in approximately 25 mL of DCM. The 50mL three-neck flasks were connected with tubing and purged with nitrogen for 10 min. Lutidinium triflate (0.0142 g, 0.055 mmol, 1.8 equiv) in 1 mL of acetonitrile was added to the reaction mixture via a Hamilton Sample Lock syringe. 1 mL of aliquot was removed from the solution of CoTPP to analyze the amount of CoTPP-NO after the reaction was stirred for 8 hours. Characterization by ^{1}H NMR spectroscopy showed that almost 0.14 equiv of Co-TPP was converted to CoTPP-NO (Figure S3).

Catalytic Nitrite Reduction with [N(afa^{Cy})$_3$Fe(OTf)]OTf (1-Cy, 0.1 equiv) with a syringe pump

A 50 mL three-neck flask was charged with NaNO$_2$ (0.0066 g, 0.096 mmol, 1.25 equiv), 1,2-diphenylhydrazine (0.014 g, 0.076 mmol, 1 equiv), 20 mg of MgSO$_4$, and 4 mL of acetonitrile. In another 50 mL three-neck flask, cobalt(II) tetraphenylporphyrine (CoTPP) (0.0515 g, 0.077 mmol, 1 equiv) was dissolved in approximately 30 mL of DCM. The 50mL three-neck flasks were connected with tubing and purged with nitrogen for 10 min. [N(afa^{Cy})$_3$Fe(OTf)]OTf (0.0072 g, 0.0077 mmol, 0.1 equiv) in 1 mL of acetonitrile was added via a Hamilton Sample Lock syringe to the mixture of NaNO$_2$ and 1,2-diphenylhydrazine. After stirring for 10 min, lutidinium triflate (0.035 g, 0.136 mmol, 1.8 equiv) in 1 mL of acetonitrile was added to the reaction mixture via a Hamilton Sample Lock syringe using a syringe pump for 6.5 hours. 0.5 mL of aliquot was removed from the solution of CoTPP to analyze the amount of CoTPP-NO after the reaction was stirred for 9 hours. Characterization by ^{1}H NMR spectroscopy showed that 0.67 equiv of CoTPP was converted to CoTPP-NO (Figure S5).

Preparation of [N(afa^{Ph})$_3$Fe(OTf)]OTf (1-Ph)

To the previously published ligand H$_3$[N(pi^{Ph})]^{27} (0.052 mg, 0.092 mmol), was added 40 mg of Fe(OTf)$_2$(MeCN)$_2$ (0.092 mmol) in acetonitrile (5 mL) and stirred at room temperature. After stirring for 1 h, solvent was removed in vacuo. The crude material was washed with dichloromethane (5 mL) to remove soluble impurities,

then recollected with tetrahydrofuran, and dried once again. Crystals suitable for X-ray diffraction (Figure S7) were grown by vapor diffusion of diethyl ether into a solution of $N(afa^{Ph})_3Fe(MeCN)(OTf)_2$ dissolved in MeCN. 74 mg of $N(afa^{Ph})_3Fe(OTf)_2$ was collected as an orange powder (0.081 mmol, 87%). ^{1}H NMR (MeCN, 21 [0]C, Figure S6): δ = 1.11, 3.40, 3.87, 6.72, 10.34, 12.07, 15.33, 20.21, 37.77, 155.29 IR = 1639 cm^{-1} (C=N). Analysis for $C_{38}H_{33}N_7O_6S_2F_6Fe \cdot 0.25\ CH_2Cl_2$: Calcd C, 48.93; H, 3.6; N, 10.44. Found C, 48.98; H, 3.56; N, 10.54. μ_{eff}: 5.59(5) μ_B.

Catalytic Nitrite Reduction with $[N(afa^{Ph})_3Fe(OTf)]OTf$ (1-Ph)

A 50 mL three-neck flask was charged with $NaNO_2$ (0.0026 g, 0.038 mmol, 1.25 equiv), 1,2-diphenylhydrazine (0.0056 g, 0.03 mmol, 1 equiv), 15 mg of $MgSO_4$, and 5 mL of acetonitrile. In another 50 mL three-neck flask, cobalt(II) tetraphenylporphyrine (CoTPP) (0.0206 g, 0.03 mmol, 1 equiv) was dissolved in approximately 25 mL of DCM. The 50mL three-neck flasks were connected with tubing and purged with nitrogen for 10 min. $[N(afa^{Ph})_3Fe(OTf)]OTf$ (0.0071 g, 0.0077 mmol, 0.25 equiv) in 1 mL of acetonitrile was added via a Hamilton Sample Lock syringe to the mixture of $NaNO_2$ and 1,2-diphenylhydrazine. After stirring for 10 min, lutidinium triflate (0.0142 g, 0.055 mmol, 1.8 equiv) in 1 mL of acetonitrile was added to the reaction mixture via a Hamilton Sample Lock syringe. 1 mL of aliquot was removed from the solution of CoTPP to analyze the amount of CoTPP-NO after the reaction was stirred for 8 hours. Characterization by ^{1}H NMR spectroscopy showed that almost 0.55 equiv of Co-TPP was converted to CoTPP-NO (Figure S8).

Preparation of $H_3[N(pi^{Ad})_3]$.

The previously synthesized $H_3(tpa^{CO})$[17] (0.250 g, 0.72 mmol), 1-adamantylamine (0.382 g, 2.20 mmol), and a stir bar were added to a 20 mL scintillation vile to which methanol (10 mL) was added. The reaction was stirred at room temperature for 18 h, after which time the product $H_3[N(pi^{Ad})_3]\cdot H_2O$ was precipitated as a tan powder. The product was collected by filtration and washed with diethyl ether (0.310 g, 0.41 mmol, 57%). $H_3[N(pi^{Ad})_3]H_2O$ was dried over mole sieves (4 Å) after dissolution in DCM. Removal of volatiles produced a light tan power. HRMS (ES[+]) calc. for $C_{48}N_7H_{64}$ (MH)[+]: 738.54, found 738.52. ^{1}H NMR (600 MHz, CDCl₃) δ = 9.43 (s, 2H, pyrrole N-*H*), 8.05 (s, 3H, imine C-*H*), 6.37 (s, 3H, pyrrole C-*H*), 6.08 (s, 3H, pyrrole C-*H*), 3.51 (s, 6H, methylene C-*H*), 2.15 (s, 9H, ada. C-*H*), 1.87 – 1.61 (m, 44H, ada. C*H₂*).^{13}C NMR (CDCl₃, 21˚C, Figure S10): δ = 29.71, 36.67, 43.45, 49.72, 56.76, 109.89, 113.21, 131.49, 145.52. IR = 1621 cm^{-1} (C=N).

Preparation of $[N(afa^{Ad})_3Fe(OTf)]OTf$ (1-Ad)

A 20 mL scintillation vial was charged with $Fe(OTf)_2(MeCN)_2$ (0.043 g, 0.100 mmol) and approximately 5 mL of tetrahydrofuran. With vigorous stirring, $H_3N(pi^{Ad})_3$ (0.073 g, 0.100 mmol) was added by difference, resulting in an instantaneous color change to yellow-orange. The mixture was stirred for 2 h, after which time volatiles were removed under reduced pressure. The resulting orange powder was washed with three, 5 mL portions of diethyl ether (0.089 g, 77%). Crystals suitable for X-ray analysis (Figure S12) were from a concentrated solution of acetonitrile with vapor diffusion of diethyl ether at room temperature to obtained acetonitrile bound species $[N(afa^{Ad})_3Fe(NCMe)]OTf_2$. ^{1}H NMR (MeCN, 21°C, Figure S11):

δ = 3.66, 4.02, 4.63, 4.86, 5.59, 14.24, 19.38, 35.76, 164.73. IR: 1635 cm^{-1} (C=N), μ_{eff} = 5.52(6) μ_B.

Catalytic Nitrite Reduction with $[N(afa^{Ad})_3Fe(OTf)](OTf)$ (1-Ad)

A 50 mL three-neck flask was charged with $NaNO_2$ (0.0026 g, 0.038 mmol, 1.25 equiv), 1,2-diphenylhydrazine (0.0056 g, 0.03 mmol, 1 equiv), 15 mg of $MgSO_4$, and 5 mL of acetonitrile. In another 50 mL three-neck flask, cobalt(II) tetraphenylporphyrine (CoTPP) (0.0206 g, 0.03 mmol, 1 equiv) was dissolved in approximately 25 mL of DCM. The 50mL three-neck flasks were connected with tubing and purged with nitrogen for 10 min. $[N(afa^{Ad})_3Fe(OTf)](OTf)$ (0.0084 g, 0.0077 mmol, 0.25 equiv) in 1 mL of acetonitrile was added via a Hamilton Sample Lock syringe to the mixture of $NaNO_2$ and 1,2-diphenylhydrazine. After stirring for 10 min, lutidinium triflate (0.0142 g, 0.055 mmol, 1.8 equiv) in 1 mL of acetonitrile was added to the reaction mixture via a Hamilton Sample Lock syringe. 1 mL of aliquot was removed from the solution of CoTPP to analyze the amount of CoTPP-NO after the reaction was stirred for 8 hours. Characterization by ^{1}H NMR spectroscopy showed that > 99% of Co-TPP was converted to CoTPP-NO (Figure S13).

Preparation of $H_3[N(pi^{Mes})_3]$

The previously synthesized $H_3(tpa^{CO})$[17] (1.0 g, 2.88 mmol) was dispersed in ethanol (100 % 12 mL). 2,4,6,-Trimethylaniline (1.2 g, 8.93 mmol) was added to the reaction mixture, followed by 6 drops of formic acid added. The reaction was stirred at 50°C for 24 hours, after which time the product $H_3[N(pi^{Mes})_3]\cdot H_2O$ was precipitated as a tan powder. $H_3[N(pi^{Mes})_3]\cdot H_2O$ was collected by filtration and washed with ethanol and acetonitrile several times in a frit (1.45 g, 2.1 mmol, 75%). To dry the $H_3[N(pi^{Mes})_3]\cdot H_2O$, mole sieves (4 Å) was added to diethyl ether solution of $H_3[N(pi^{Mes})_3]\cdot H_2O$ overnight. After evaporating solvents to dryness, the $H_3[N(pi^{Mes})_3]\cdot H_2O$ was recrystallized from diethyl ether/MeCN (2:1) at -35˚C. Analysis (calcd., found for $C_{45}H_{51}N_7\cdot CH_3CN$): C (77.23, 76.84), H (7.45, 7.33), N (15.33, 15.38). ^{1}H NMR (C₆D₆, 21˚C, Figure S14): δ = 2.17 (s, 18H, CH₃-Mes), 2.20 (s, 9H, CH₃-Mes), 3.18 (s, 6H, -CH₂), 6.12 (d, *J* = 3.2 Hz, 3H, pyr-CH), 6.40 (d, *J* = 3.2 Hz, 3H, pyr-CH), 6.82 (s, 6H, Mes-CH), 7.65 (s, 3H, imine-CH), 9.52 (s, 3H, -NH). ^{13}C NMR (CDCl₃, 21˚C, Figure S15): δ = 18.50, 20.87, 50.26, 110.29, 115.97, 127.83, 128.81, 130.69, 132.80, 133.38, 148.56, 152.21. IR = 1621 cm^{-1} (C=N).

Preparation of $[N(afa^{Mes})_3Fe(OTf)]OTf$ (1-Mes)

A 20 mL scintillation vial was charged with $Fe(OTf)_2(MeCN)_2$ (0.043 g, 0.100 mmol) and approximately 10 mL of tetrahydrofuran. With vigorous stirring, $H_3N(pi^{Mes})_3$ (0.070 g, 0.101 mmol) was added by difference, resulting in an instantaneous color change to orange. The mixture was stirred for one hour, after which time solvents were removed under reduced pressure. Following removal of volatiles, the orange powder was washed with diethyl ether three times (0.101 g, 97 %). Crystals suitable for X-ray analysis were from a concentrated solution of tetrahydrofuran layered with diethyl ether at room temperature. Analysis (calcd., found for $FeC_{47}H_{51}N_7S_2F_6O_6$): C (54.08, 54.43), H (4.92, 5.01), N (9.39, 9.39). ^{1}H NMR (MeCN, 21°C, Figure S16): ^{1}H NMR (MeCN, 21°C, Figure S16) δ 157.77, 155.39, 153.39, 149.65, 38.59, 38.21, 36.55, 36.30, 21.20, 20.57, 18.94, 18.24, 17.61, 13.69, 10.00, 7.93, 7.73, 7.31, 4.76,

4.08, 3.92, 3.25, 2.72, 2.28, 0.95, 0.45, 0.36, -2.53, -2.93. IR: 1621, 1636 cm^{-1}(C=N), 3193 cm^{-1}(NH). μ_{eff} = 5.52(6) μ_B.

Catalytic Nitrite Reduction with [N(afa^{Mes})$_3$Fe(OTf)]OTf (1-Mes)

A 50 mL three-neck flask was charged with NaNO$_2$ (0.0026 g, 0.038 mmol, 1.25 equiv), 1,2-diphenylhydrazine (0.0056 g, 0.03 mmol, 1 equiv), 15 mg of MgSO$_4$, and 5 mL of acetonitrile. In another 50 mL three-neck flask, cobalt(II) tetraphenylporphyrine (CoTPP) (0.0206 g, 0.03 mmol, 1 equiv) was dissolved in approximately 25 mL of DCM. The 50mL three-neck flasks were connected with tubing and purged with nitrogen for 10 min. [N(afa^{Mes})$_3$Fe(OTf)]OTf (0.008 g, 0.0077 mmol, 0.25 equiv) in 1 mL of acetonitrile was added via a Hamilton Sample Lock syringe to the mixture of NaNO$_2$ and 1,2-diphenylhydrazine. After stirring for 10 min, lutidinium triflate (0.0142 g, 0.055 mmol, 1.8 equiv) in 1 mL of acetonitrile was added to the reaction mixture via a Hamilton Sample Lock syringe. 1 mL of aliquot was removed from the solution of CoTPP to analyze the amount of CoTPP-NO after the reaction was stirred for 8 hours. Characterization by ^{1}H NMR spectroscopy showed that all Co-TPP was converted to CoTPP-NO (Figure S17). Analysis for CoTPP-NO: ^{1}H NMR (CDCl$_3$, 25°C): δ = 8.91, 8.18, 7.74 ppm. IR = 1693 cm^{-1} (NO).

Nitrite reduction with 1-Mes to generate [N(afa^{Mes})$_2$(Pi^{Mes})FeOH]OTf (2-Mes)

A 20 mL scintillation vial was charged with [N(afa^{Mes})$_3$Fe(OTf)](OTf) (0.102 g, 0.097 mmol) in an approximately 10 mL of acetonitrile. With vigorous stirring, tetrabutylammonium nitrite [N^{n}Bu$_4$][NO$_2$] (0.028 g, 0.100 mmol) was added as a solid. The mixture was stirred for two hours, after which time solvent was removed under reduced pressure. The product was recrystallized from concentrated THF/benzene solution layered with slow diffusion of diethyl ether (0.068 g, 78 %) (Figure S18). Analysis (calcd., found for C$_{46}$H$_{51}$O$_4$N$_7$FeSF$_3$·0.5C$_5$H$_6$): C (61.96, 61.94), H (5.73, 5.74), N (10.32, 10.14). ^{19}F NMR (CD$_3$CN, 21 °C): δ = −79.63 (SO$_3$CF$_3$). IR: 1634, 1651 cm^{-1} (C=N) μ_{eff} = 5.94(9) μ_B.

Reduction of [N(afa^{Mes})$_2$(Pi^{Mes})FeOH](OTf) (2-Mes) to [N(afa^{Mes})$_3$Fe]OTf$_2$ (1-Mes)

A 20 mL scintillation vial was charged with [N(afa^{Mes})$_2$(Pi^{Mes})FeOH](OTf) (2-Mes) (0.018 g, 0.020 mmol) and DPH (0.022 g, 0.012 mmol) in 3 mL of MeCN. HOTf (0.004 g, 0.032mmol) was added and stirred for 2 hours. In order to quantify the amount of water formed during the reaction, three aliquots of 0.5 mL were removed from the vial using a Hamilton Sample Lock syringe and analyzed by Karl Fischer titration (Table S1). The solvent was removed under reduced pressure and the resulting orange oil. Characterization by ^{1}H NMR spectroscopy (Figure S19) revealed a clean conversion of 2-Mes to 1-Mes. (0.019 g, 0.0182 mmol, 91 %).

Preparation of [N(afa^{Mes})$_2$(pi^{Mes})FeOH$_2$](OTf)$_2$ (3-Mes) Step (A-1, Scheme 3)

A 20 mL scintillation vial was charged with [N(afa^{Mes})$_2$(Pi^{Mes})FeOH](OTf) (2-Mes) (0.018 g, 0.020 mmol) in an approximately 3 mL of MeCN. HOTf (1.5 equiv 0.045 g, 0.03 mmol) was added and stirred for 10 min. The resulting red-brown

solution was analyzed by mass spectrometry using a Hamilton Sample Lock syringe. Characterization by ^{1}H NMR spectroscopy (Figure S20) revealed a formation of new paramagnetic compound. LRMS (ESI) (m/z): [M]$^{2+}$ calcd. for C$_{45}$H$_{52}$FeN$_7$O ([N(afa^{Mes})$_2$(pi^{Mes})FeOH$_2$]$^{2+}$) 381.18, found: 381.1 (Figure S21) ^{19}F NMR (CD$_3$CN, 21 °C): δ = −70.70 (SO$_3$CF$_3$). IR: 1622, 1649 cm^{-1} (C=N), 3205 cm^{-1} (OH).

Reduction of [N(afa^{Mes})$_2$(pi^{Mes})FeOH$_2$](OTf)$_2$ (3-Mes) to 1-Mes. (A-2, Scheme 3)

In a solution of [N(afa^{Mes})$_2$(pi^{Mes})FeOH$_2$](OTf)$_2$ (3-Mes) prepared in situ, 0.6 equiv of DPH (0.022 g, 0.012 mmol) was added and stirred for 2 hour. In order to quantify the amount of water formed during the reaction, three aliquots of 0.5 mL were removed from the vial using a Hamilton Sample Lock syringe and analyzed by Karl Fischer titration (Table S1). Characterization by ^{1}H NMR spectroscopy confirmed the formation of complex 1-Mes (0.0155 g, 0.015 mmol, 74%).

Reduction of [N(afa^{Mes})$_2$(Pi^{Mes})FeOH]OTf (2-Mes) to complex N(afa^{Mes})(pi^{Mes})$_2$Fe(OH)$_2$ (4-Mes), (B-1, Scheme 3)

A 20 mL scintillation vial was charged with [N(afa^{Mes})$_2$(pi^{Mes})FeOH]OTf (2-Mes) (0.018 g, 0.020 mmol) in an approximately 3 mL of THF. KC$_8$ (0.0034 g, 0.026 mmol) was added as a solid and stirred for 10 min. The reaction mixture was filtered over Celite to remove graphite and the solvent was reduced under pressure. The resulting brown solid was dissolved in benzene and filtered over Celite to get rid of KOTf. After the solvent was reduced under pressure, the resulting powder was confirmed the formation of 4-Mes by ^{1}H NMR spectroscopy (0.0125 g, 0.016 mmol, 82%) (Figure S22).

Reaction of N(afa^{Mes})(pi^{Mes})$_2$Fe(OH$_2$) (4-Mes) with HOTf to form [N(afa^{Mes})$_3$FeOTf]OTf (1-Mes). (B-2, Scheme 3)

A 20 mL scintillation vial was charged with N(afa^{Mes})(pi^{Mes})$_2$Fe(OH$_2$) (0.015 g, 0.020 mmol) in 3 mL of MeCN. HOTf (triflic acid) (2.2 equiv 0.065 g, 0.043 mmol) was added and the reaction was stirred for 30 min. In order to quantify the amount of water formed during the reaction, three aliquots of 0.5 mL were removed from the vial using a Hamilton Sample Lock syringe and analyzed by Karl Fischer titration (Table S1). The solution was filtered over Celite and the solvent was removed under reduced pressure. The yellow oil was washed with benzene to get rid of a small amount of acidified ligand formed during the reaction. Characterization by ^{1}H NMR spectroscopy revealed a conversion of 4-Mes to 1-Mes (0.019 g, 0.018 mmol, 91%).

Alternative preparation of N(afa^{Mes})(pi^{Mes})$_2$Fe(OH$_2$) (4-Mes)

H$_3$[N(pi^{Mes})$_3$] (0.070 g, 0.101 mmol) was deprotonated by addition of 2.2 equivalent KH (0.009 g, 0.22 mmol) to an approximately 10 mL of THF solution. After it was stirred for three hours at room temperature, the mixture was filtered through Celite to remove excess KH. Addition of deprotonated ligand to the FeCl$_2$ (0.013 g, 0.0103 mmol) slurry in THF resulted in a color change from colorless to yellow. After stirring for overnight until all FeCl$_2$ was consumed, the reaction mixture was filtered through Celite to remove KCl and the solvents were removed under reduced pressure. Crystals suitable for X-ray analysis were grown at room temperature from a concentrated

solution of THF layered with pentane (0.034g, 45%). Analysis (calcd., found for $C_{45}H_{51}FeN_7O$) C (70.95, 70.59), H (6.75, 6.81), N (12.87, 12.69). IR: 1643, 1616 cm^{-1} (C=N).

Alternative Synthesis of $N(afa^{Mes})(pi^{Mes})_2Fe(OH_2)$ (4-Mes)

A 20 mL scintillation vial was charged with complex **2-Mes** (0.050 g, 0.048 mmol) in an approximately 5 mL of THF. Li_2O (2.5 equiv, 0.0036 g, 0.12 mmol) was added as solid to the aforementioned solution. The mixture was stirred overnight at room temperature, resulting in orange solution. The solution was filtered over Celite to remove excess Li_2O and the solvent was removed under reduced pressure. The residual yellow powder was washed with acetonitrile and dried under vacuum, resulting in an isolation of **4-Mes** as orange powder (0.035 g, 0.045 mmol, 94 %), identified via ^{1}H NMR spectroscopy.

Computational Methods. DFT calculations were carried out using the dispersion-corrected hybrid exchange-correlation functional ωB97XD,[49] implemented in the Gaussian09 software.[50] To describe the C and H atoms, the 6-31G(d,p) basis set with polarization functions was employed, while the same basis set with added diffuse *p*-functions was used in the description of the more electronegative N and O atoms. For the Fe metal center, the effective core potential Lanl2dz[51,52] with an additional *f*-polarization function (exponent: 2.462)[53] was used. Fe(III) complexes were modelled as high-spin with a total spin S = 5/2, based on the magnetic moments measured experimentally. Geometry optimizations were performed in vacuum without imposing any symmetry constraints, and the nature of all the stationary points was verified through vibrational frequency analysis. As expected, all the energy minima were confirmed to display only real vibrational frequencies, whereas transition states were found to exhibit one single imaginary frequency. For the latter, geometry relaxations along the reaction coordinate were also carried out to confirm they connect the corresponding reaction energy minima.

The effect of the solvents employed in experiments (MeCN, ε = 35.69; THF, ε = 7.43) were introduced via single-point calculations on the optimized geometries in vacuum using the implicit SMD solvation model.[54] The calculated energies with the above basis sets (BS1) were refined via single-point solvent calculations using an extended triple-ζ basis set for all atoms, *i.e.* 6-311G(d,p) for C and H, 6-311+G(d,p) for N and O, and Lanl2tz for Fe, denoted as BS2. The reported Gibbs energies in solution were calculated by adding the gas-phase Gibbs corrections obtained with BS1 to the potential energies in solution computed with BS2. Additionally, geometry optimizations using the implicit SMD solvation model were carried out for the *closed* structures of the oxo and hydroxo complexes with the Cy ligand, leading to negligible structural (bond lengths involving the metal center differ by only *ca.* 0.02 Å) and $\Delta G_{(MeCN)}$ variations (ca. <0.3 kcal mol^{-1}), which do not affect the overall conclusions of this work.

Natural bond orbital (NBO) analysis on selected donor-acceptor interactions was performed using the software NBO 6.0.[55] The analysis of the non-covalent interactions (NCIs) between the ligands and the oxo and hydroxo moieties were assessed by means of the Critic2 software,[56] as reported elsewhere.[57,58] The wavefunction used in the NCI analysis was inherited from the geometry optimizations performed in vacuum with Gaussian09.

ASSOCIATED CONTENT

Supporting Information

Spectral details.

Crystallographic details for **compounds 1-Mes, 2-Mes, 4-Mes, 1-Ph and 1-Ad** are available from the Cambridge structural database, CCDC 1842647-1842651. Additional computational information and supplementary Figures. All the DFT data underlying this work, including the cartesian coordinates and energies of all the modelled structures, is openly accessible via the following ioChem-BD online dataset: https://iochem-bd.bsc.es/browse/review-collection/100/198140/b675c48fa291d80adfd6ea8c

The supporting information is available free of charge on the ACS Publication website at DOI:
Experimental data (PDF)

AUTHOR INFORMATION

Corresponding Author

*Email: garciamm@tcd.ie ; fout@illinois.edu
ORCID
Max García-Melchor: 0000-0003-1348-4692
Alison R. Fout: 0000-0002-4669-5835
Notes
The authors declare no competing financial interests.

REFERENCES

(1)   Kuypers, M. M. M.; Marchant, H. K.; Kartal, B. The Microbial Nitrogen-Cycling Network. *Nat. Rev. Microbiol.* **2018**, *16* (5), 263–276.

(2)   Maia, L. B.; Moura, J. J. G. How Biology Handles Nitrite. *Chem. Rev.* **2014**, *114* (10), 5273–5357.

(3)   Heinecke, J.; Ford, P. C. Mechanistic Studies of Nitrite Reactions with Metalloproteins and Models Relevant to Mammalian Physiology. *Coord. Chem. Rev.* **2010**, *254* (3–4), 235–247.

(4)   Cosby, K.; Partovi, K. S.; Crawford, J. H.; Patel, R. P.; Reiter, C. D.; Martyr, S.; Yang, B. K.; Waclawiw, M. A.; Zalos, G.; Xu, X.; et al. Nitrite Reduction to Nitric Oxide by Deoxyhemoglobin Vasodilates the Human Circulation. *Nat. Med.* **2003**, *9* (12), 1498–1505.

(5)   Omar, S. A.; Webb, A. J. Nitrite Reduction and Cardiovascular Protection. *J. Mol. Cell. Cardiol.* **2014**, *73*, 57–69.

(6)   Gladwin, M. T.; Schechter, A. N.; Kim-Shapiro, D. B.; Patel, R. P.; Hogg, N.; Shiva, S.; Cannon, R. O.; Kelm, M.; Wink, D. A.; Espey, M. G.; et al. The Emerging Biology of the Nitrite Anion. *Nat. Chem. Biol.* **2005**, *1* (6), 308–314.

(7)   Camargo, J. A.; Alonso, Á. Ecological and Toxicological Effects of Inorganic Nitrogen Pollution in Aquatic Ecosystems: A Global Assessment. *Environ. Int.* **2006**, *32* (6), 831–849.

(8)   Camargo, J. A.; Alonso, A.; Salamanca, A. Nitrate Toxicity to Aquatic Animals: A Review with New Data for Freshwater Invertebrates. *Chemosphere* **2005**, *58* (9), 1255–1267.

(9)   Ranghino, G.; Scorza, E.; Sjogren, T.; Williams, P. A.; Ricci, M.; Hajdu, J. Quantum Mechanical Interpretation of Nitrite Reduction by Cytochrome Cd1 Nitrite Reductase from Paracoccus Pantotrophus.

Biochemistry **2000**, *39* (36), 10958–10966.

(10) Sundararajan, M.; Neese, F. Distal Histidine Modulates the Unusual O-Binding of Nitrite to Myoglobin: Evidence from the Quantum Chemical Analysis of EPR Parameters. *Inorg. Chem.* **2015**, *54* (15), 7209–7217.

(11) Zahran, Z. N.; Chooback, L.; Copeland, D. M.; West, A. H.; Richter-Addo, G. B. Crystal Structures of Manganese- and Cobalt-Substituted Myoglobin in Complex with NO and Nitrite Reveal Unusual Ligand Conformations. *J. Inorg. Biochem.* **2008**, *102* (2), 216–233.

(12) Xu, N.; Yi, J.; Richter-Addo, G. B. Linkage Isomerization in Heme-NOx Compounds: Understanding NO, Nitrite, and Hyponitrite Interactions with Iron Porphyrins. *Inorg. Chem.* **2010**, *49* (14), 6253–6266.

(13) Cutruzzola, F.; Brown, K.; Wilson, E. K.; Bellelli, A.; Arese, M.; Tegoni, M.; Cambillau, C.; Brunori, M. The Nitrite Reductase from Pseudomonas Aeruginosa: Essential Role of Two Active-Site Histidines in the Catalytic and Structural Properties. *Proc. Natl. Acad. Sci. U. S. A.* **2001**, *98* (5), 2232–2237.

(14) Farver, O.; Kroneck, P. M. H.; Zumft, W. G.; Pecht, I. Allosteric Control of Internal Electron Transfer in Cytochrome Cd1 Nitrite Reductase. *Proc. Natl. Acad. Sci. U. S. A.* **2003**, *100* (13), 7622–7625.

(15) Park, Y. J.; Matson, E. M.; Nilges, M. J.; Fout, A. R. Exploring Mn-O Bonding in the Context of an Electronically Flexible Secondary Coordination Sphere: Synthesis of a Mn(Iii)-Oxo. *Chem. Commun.* **2015**, *51* (25), 5310–5313.

(16) Sanders, B. C.; Hassan, S. M.; Harrop, T. C. NO2– Activation and Reduction to NO by a Nonheme Fe(NO2)2 Complex. *J. Am. Chem. Soc.* **2014**, *136* (29), 10230–10233.

(17) Ching, W.-M.; Chuang, C.-H.; Wu, C.-W.; Peng, C.-H.; Hung, C.-H. Facile Nitrite Reduction and Conversion Cycle of {Fe(NO)}6/7 Species: Chemistry of Iron N-Confused Porphyrin Complexes via Protonation/Deprotonation. *J. Am. Chem. Soc.* **2009**, *131* (23), 7952–7953.

(18) Uyeda, C.; Peters, J. C. Selective Nitrite Reduction at Heterobimetallic CoMg Complexes. *J. Am. Chem. Soc.* **2013**, *135* (32), 12023–12031.

(19) Burns, K. T.; Marks, W. R.; Cheung, P. M.; Seda, T.; Zakharov, L. N.; Gilbertson, J. D. Uncoupled Redox-Inactive Lewis Acids in the Secondary Coordination Sphere Entice Ligand-Based Nitrite Reduction. *Inorg. Chem.* **2018**, *57* (16), 9601–9610.

(20) Kwon, Y. M.; Delgado, M.; Zakharov, L. N.; Seda, T.; Gilbertson, J. D. Nitrite Reduction by a Pyridinediimine Complex with a Proton-Responsive Secondary Coordination Sphere. *Chem. Commun.* **2016**, *52* (73), 11016–11019.

(21) Harris, T. D.; Betley, T. A. Multi-Site Reactivity: Reduction of Six Equivalents of Nitrite To Give an Fe6(NO)6 Cluster with a Dramatically Expanded Octahedral Core. *J. Am. Chem. Soc.* **2011**, *133* (35), 13852–13855.

(22) Suslick, K. S.; Watson, R. A. Photochemical Reduction of Nitrate and Nitrite by Manganese and Iron Porphyrins. *Inorg. Chem* **1991**, *30*, 912–919.

(23) Matson, E. M.; Park, Y. J.; Fout, A. R. Facile Nitrite Reduction in a Non-Heme Iron System: Formation of an Iron(III)-Oxo. *J. Am. Chem. Soc.* **2014**, *136* (50), 17398–17401.

(24) Moore, C. M.; Szymczak, N. K. Nitrite Reduction by Copper through Ligand-Mediated Proton and Electron Transfer. *Chem. Sci.* **2015**, *6* (6), 3373–3377.

(25) Ford, C. L.; Park, Y. J.; Matson, E. M.; Gordon, Z.; Fout, A. R. A Bioinspired Iron Catalyst for Nitrate and Perchlorate Reduction. *Science (80-.).* **2016**, *354* (6313), 741–743.

(26) Drummond, M. J.; Miller, T. J.; Ford, C. L.; Fout, A. R. Catalytic Perchlorate Reduction Using Iron: Mechanistic Insights and Improved Catalyst Turnover. *ACS Catal.* **2020**, *10* (5), 3175–3182.

(27) Silaghi-Dumitrescu, R. Linkage Isomerism in Nitrite Reduction by Cytochrome Cd1nitrite Reductase. *Inorg. Chem.* **2004**, *43* (12), 3715–3718.

(28) Wang, J.; Zhao, Y.; Lee, P.-H.; Wu, K. Computational Analysis of Non-Heme Iron–Oxo Formation by Direct NO Release in Nitrite Reduction. *Phys. Chem. Chem. Phys.* **2019**, *21* (12), 6643–6650.

(29) Stroka, J. R.; Kandemir, B.; Matson, E. M.; Bren, K. L. Electrocatalytic Multielectron Nitrite Reduction in Water by an Iron Complex. *ACS Catal.* **2020**, *10* (23), 13968–13972.

(30) He, D.; Li, Y.; Ooka, H.; Go, Y. K.; Jin, F.; Kim, S. H.; Nakamura, R. Selective Electrocatalytic Reduction of Nitrite to Dinitrogen Based on Decoupled Proton–Electron Transfer. *J. Am. Chem. Soc.* **2018**, *140* (6), 2012–2015.

(31) Cioncoloni, G.; Roger, I.; Wheatley, P. S.; Wilson, C.; Morris, R. E.; Sproules, S.; Symes, M. D. Proton-Coupled Electron Transfer Enhances the Electrocatalytic Reduction of Nitrite to NO in a Bioinspired Copper Complex. *ACS Catal.* **2018**, *8* (6), 5070–5084.

(32) Cheung, P. M.; Burns, K. T.; Kwon, Y. M.; Deshaye, M. Y.; Aguayo, K. J.; Oswald, V. F.; Seda, T.; Zakharov, L. N.; Kowalczyk, T.; Gilbertson, J. D. Hemilabile Proton Relays and Redox Activity Lead to {FeNO}x and Significant Rate Enhancements in NO2– Reduction. *J. Am. Chem. Soc.* **2018**, *140* (49), 17040–17050.

(33) Toth, J. E.; Anson, F. C. Electrocatalytic Reduction of Nitrite and Nitric Oxide to Ammonia with Iron-Substituted Polyoxotungstates. *J. Am. Chem. Soc.* **1989**, *111* (7), 2444–2451.

(34) Barley, M. H.; Rhodes, M. R.; Meyer, T. J. Electrocatalytic Reduction of Nitrite to Nitrous Oxide and Ammonia Based on the N-Methylated, Cationic Iron Porphyrin Complex [FeIII(H2O)(TMPyP)]5+. *Inorg. Chem.* **1987**, *26* (11), 1746–1750.

(35) Barley, M. H.; Meyer, T. J. Electrocatalytic Reduction of Nitrite to Ammonia Based on a Water-Soluble Iron Porphyrin. *J. Am. Chem. Soc.* **1986**, *108* (19), 5876–5885.

(36) Lee, J.; Hur, Y. G.; Kim, M. S.; Lee, K. Y. Catalytic Reduction of Nitrite in Water over Ceria- and Ceria-Zirconia-Supported Pd Catalysts. *J. Mol. Catal. A Chem.* **2015**, *399*, 48–52.

(37) Matson, E. M.; Park, Y. J.; Bertke, J. A.; Fout, A. R. Synthesis and Characterization of M(II) (M = Mn, Fe and Co) Azafulvene Complexes and Their X3- Derivatives. *Dalt. Trans.* **2015**, *44* (22).

(38) Gordon, Z.; Drummond, M. J.; Matson, E. M.; Bogart, J. A.; Schelter, E. J.; Lord, R. L.; Fout, A. R. Tuning the Fe(II/III) Redox Potential in Nonheme Fe(II)-Hydroxo Complexes through Primary and Secondary Coordination Sphere Modifications. *Inorg. Chem.* **2017**, *56* (9).

(39) Matson, E. M.; Bertke, J. A.; Fout, A. R. Isolation of Iron(II) Aqua and Hydroxyl Complexes Featuring a Tripodal H-Bond Donor and Acceptor Ligand. *Inorg. Chem.* **2014**, *53* (9), 4450–4458.

(40) Wayland, B.; Minkiewicz, J. V. Reactions of Nitric Oxide with Cobalt (I1) Tetraphenylporphyrin : Lob0 A. **1976**, No. I, 1015–1016.

(41) Matson, E.; Park, Y.; Fout, A. Facile Nitrite Reduction in a Non-Heme Iron System: Formation of an Iron (III)-Oxo. *J. Am. Chem. Soc.* **2014**, *136* (Iii), 17398.

(42) Ford, C. L.; Park, Y. J.; Matson, E. M.; Gordon, Z.; Fout, A. R. A Bioinspired Iron Catalyst for Nitrate to Perchlorate Reduction. *Science (80-.).* **2015**, *354* (6313), 741–743.

(43) Perrin, D. D. Dissociation Contants of Inorganic Acids and Bases in Aqueous Solution. *Pure Appl. Chem.* **1969**, *20* (2).

(44) Klein, A.; Neugebauer, M.; Krest, A.; Lüning, A.; Garbe, S.; Arefyeva, N.; Schlörer, N. Five Coordinate Platinum(II) in [Pt(Bpy)(Cod)(Me)][SbF6]: A Structural and Spectroscopic Study. *Inorganics* . 2015.

(45) MacBeth, C. E.; Golombek, A. P.; Young, V. G.; Yang, C.; Kuczera, K.; Hendrich, M. P.; Borovik, A. S. O2 Activation by Nonheme Iron Complexes: A Monomeric Fe(III)-Oxo Complex Derived From O2. *Science (80-.).* **2000**, *289* (5481), 938.

(46) Contreras-García, J.; Johnson, E. R.; Keinan, S.; Chaudret, R.; Piquemal, J.-P.; Beratan, D. N.; Yang, W. NCIPLOT: A Program for Plotting Non-Covalent Interaction Regions. *J. Chem. Theory Comput.* **2011**, *7* (3), 625–632.

(47) The same effect can be observed in the X-ray structures obtained for 2-Cy (oxo complex; Fe-N1 = 2.3082(11) Å, see R. [23]) and 2-M. (OH complex; F. = 2. 2499(15. Å.

(48) Curley, J. J.; Bergman, R. G.; Tilley, T. D. Preparation and Physical Properties of Early-Late Heterobimetallic Compounds Featuring Ir-M Bonds (M = Ti, Zr, Hf). *Dalt. Trans.* **2012**, *41* (1), 192–200.

(49) Chai, J.-D.; Head-Gordon, M. Long-Range Corrected Hybrid Density Functionals with Damped Atom–Atom Dispersion Corrections. *Phys. Chem. Chem. Phys.* **2008**, *10* (44), 6615–6620.

(50) Frisch, M. J.; Trucks, G. W.; Schlegel, H. B.; Scuseria, G. E.; Robb, M. A.; Cheeseman, J. R.; Scalmani, G.; Barone, V.; Petersson, G. A.; Nakatsuji, H.; Li, X.; Caricato, M.; Marenich, A. V.; Bloino, J.; Janesko, B. G.; Gomperts, R.; Mennucci, B.; Hratch, D. J. Gaussian 09, Revision E.01. **2009**, *Gaussian*,.

(51)   Hay, P. J.; Wadt, W. R. Ab Initio Effective Core Potentials for Molecular Calculations. Potentials for the Transition Metal Atoms Sc to Hg. *J. Chem. Phys.* **1985**, *82* (1), 270–283.

(52)   Hay, P. J.; Wadt, W. R. Ab Initio Effective Core Potentials for Molecular Calculations. Potentials for K to Au Including the Outermost Core Orbitals. *J. Chem. Phys.* **1985**, *82* (1), 299–310.

(53)   Ehlers, A. W.; Böhme, M.; Dapprich, S.; Gobbi, A.; Höllwarth, A.; Jonas, V.; Köhler, K. F.; Stegmann, R.; Veldkamp, A.; Frenking, G. A Set of F-Polarization Functions for Pseudo-Potential Basis Sets of the Transition Metals ScCu, YAg and LaAu. *Chem. Phys. Lett.* **1993**, *208* (1–2), 111–114.

(54)   Marenich, A. V; Cramer, C. J.; Truhlar, D. G. Universal Solvation Model Based on Solute Electron Density and on a Continuum Model of the Solvent Defined by the Bulk Dielectric Constant and Atomic Surface Tensions. *J. Phys. Chem. B* **2009**, *113* (18), 6378–6396.

(55)   Glendening, E. D.; Landis, C. R.; Weinhold, F. NBO 6.0: Natural Bond Orbital Analysis Program. *J. Comput. Chem.* **2013**, *34* (16), 1429–1437.

(56)   Otero-de-la-Roza, A.; Johnson, E. R.; Luaña, V. Critic2: A Program for Real-Space Analysis of Quantum Chemical Interactions in Solids. *Comput. Phys. Commun.* **2014**, *185* (3), 1007–1018.

(57)   Kuznetsova, V. A.; Mates-Torres, E.; Prochukhan, N.; Marcastel, M.; Purcell-Milton, F.; O'Brien, J.; Visheratina, A. K.; Martinez-Carmona, M.; Gromova, Y.; Garcia-Melchor, M.; et al. Effect of Chiral Ligand Concentration and Binding Mode on Chiroptical Activity of CdSe/CdS Quantum Dots. *ACS Nano* **2019**, *13* (11), 13560–13572.

(58)   Sahm, C. D.; Mates-Torres, E.; Eliasson, N.; Sokołowski, K.; Wagner, A.; Dalle, K. E.; Huang, Z.; Scherman, O. A.; Hammarström, L.; García-Melchor, M.; et al. Imidazolium-Modification Enhances Photocatalytic CO2 Reduction on ZnSe Quantum Dots. *Chem. Sci.* **2021**, *12* (26), 9078–9087.